Simulating Compressible Turbulent Flow with the PPM Gas Dynamics Scheme

David H. Porter and Paul R. Woodward
University of Minnesota, LCSE

1. Introduction

The PPM gas dynamics scheme is described in detail elsewhere in this book (see also [1-5]). Here we review applications of PPM to turbulent flow problems. In particular, we will focus our attention on simulations of homogeneous, compressible, periodic, decaying turbulence. The motivation for this focus is that if the phenomenon of turbulence is indeed universal, we should find within this single problem a complete variety of particular circumstances. If we choose to ignore any potential dependence on the gas equation of state, choosing to adopt the gamma-law with $\gamma = 1.4$ that applies to air, we are then left with a one-parameter family of turbulent flows. This single parameter is the rms Mach number of the flow. We note that a decaying turbulent flow that begins at, say, Mach 1 will, as it decays, pass through all Mach numbers between that value and zero. Of course, we will have arbitrary possible entropy variations to deal with, but turbulence itself will tend to mix different entropy values, so that these entropy variations may not prove to be so important as we might think. In all our simulations of such homogeneous turbulence, we begin the simulation with a uniform state of density and sound speed unity and average velocity zero. We perturb this uniform state with randomly selected sinusoidal velocity variations sampled from a distribution peaked on a wavelength equal to half that of our periodic cubical simulation domain. The PPM simulations of this type that will be reviewed here have the amplitudes of these velocity variations chosen in order to achieve an initial rms Mach number of either ½ or unity.

We exploit the numerical dissipation of PPM, which is strongly targeted at the very smallest scales that can be described on our grid. This type of viscosity allows us to have in our simulations the largest possible dynamic range of scales of motion that is essentially unaffected by viscosity of any kind, either numerical or real. The idea here is that information will pass preferentially down the spectrum from larger to smaller scales of motion. Therefore, as long as we dissipate any small-scale motions into the proper amount of heat at the proper places and the proper times, we should be able to compute the dynamics of the larger scales correctly and accurately. In essence, were this not so, then there would be no hope to simulate the dynamics of a turbulent flow without computing all the motions on all the scales, however small. Nevertheless, we demand a consistency with this assumption from the results of our simulations, and this consistency is, thankfully, observed.

2. Large-Scale Simulations of Turbulent Flows in 3D

Together with our collaborator, Annick Pouquet, we decided in 1991 to exploit the high resolving power of our PPM gas dynamics scheme and the power of the University of Minnesota's Cray-2 supercomputer to simulate decaying, homogeneous, compressible turbulence in 3D [6]. We initialized the flow on a periodic, cubical domain of 256^3 grid cells so that the rms Mach number of the flow was unity. Because of Kolmogorov's compelling arguments based upon dimensional analysis and self-similarity [7], we expected to see a $k^{-5/3}$ velocity power spectrum develop. Instead, what we observed was a k^{-1} behavior between the energy containing scales and the scales on which the numerical dissipation of PPM came into play [8,9]. The Kolmogorov behavior was nevertheless present as the spectrum decayed, since the spectra at different times, when plotted together on the same graph, traced out a clear envelope with a $k^{-5/3}$ slope. This result was a surprise, since we knew from separate measurements of the effective viscosity of PPM [10,11] that all scales above 12, or at the most 16, grid cell widths were essentially inviscid. This was our first introduction to a physical effect, which we later clearly showed occurs with the Navier-Stokes viscosity as well, of a pile-up of kinetic energy near the end of the turbulent cascade. An argument offered by Jack Herring at the time was that the removal of kinetic energy on the very smallest scales supported by the computational grid inhibited scales just larger than this from transferring their energy through nonlinear interactions with smaller scales. In earlier 2-D simulations of homogeneous, compressible turbulence with PPM [8], we had observed no such effect near the end of the spectrum. The flattening of the near-dissipation-range spectrum occurs only in 3D, and only in the solenoidal component of the velocity field.

In 1992, we were able to clarify this process of flattening of the velocity power spectrum just before the dissipation range of scales is reached. Using the University of Minnesota's new Connection Machine at the Army High Performance Computing Research Center, we were able to expand the grid of our earlier 256^3 simulation to 512^3 cells. At last a short segment of the Kolmogorov inertial range emerged [12-14]. We were able to see that for the PPM dissipation the Kolmogorov inertial range extends to a shortest disturbance wavelength of about 32 grid cell widths. This scale marks the end of the indirect effects of the PPM dissipation rather than of its direct effects, since the propagation with PPM of a 16-cell sinusoidal velocity disturbance is very accurate over the brief duration of any of these turbulence simulations. From this work, we concluded that to study the statistics of the inertial range of turbulence, we needed a truly enormous grid, since with only 512^3 cells our inertial range was only about a factor of 3 in length.

With a dissipation such as the Navier-Stokes dissipation, which acts significantly on much larger scales than the PPM dissipation, the inertial range on a 512^3 grid would be even smaller. Indeed, several years later we performed a resolution study with both PPM-Euler and PPM-Navier-Stokes methods. This study used resolved Navier-Stokes simulations, for which the velocity power spectrum does not change upon a grid refinement if the coefficient of viscosity is held constant. We discovered that on a 512^3 grid such a Navier-Stokes simulation of decaying, Mach ½ turbulence reveals no inertial range at all [26]. The flattening of the spectrum before the dissipation range in Navier-Stokes flows was confirmed in 2002 by a Japanese group using the Earth Simulator to perform Navier-Stokes simulations of decaying homogeneous turbulence on grids up to 4096^3 [32].

In 1993 our quest for a machine that could simulate turbulence on a 1024^3 grid led us to collaborate with Silicon Graphics [15]. A cluster of multiprocessor SGI machines was built for us temporarily in the Silicon Graphics manufacturing facility. The combined cluster gave a sustained computational performance of 5 Gflops, which was not a record at the time. However, the

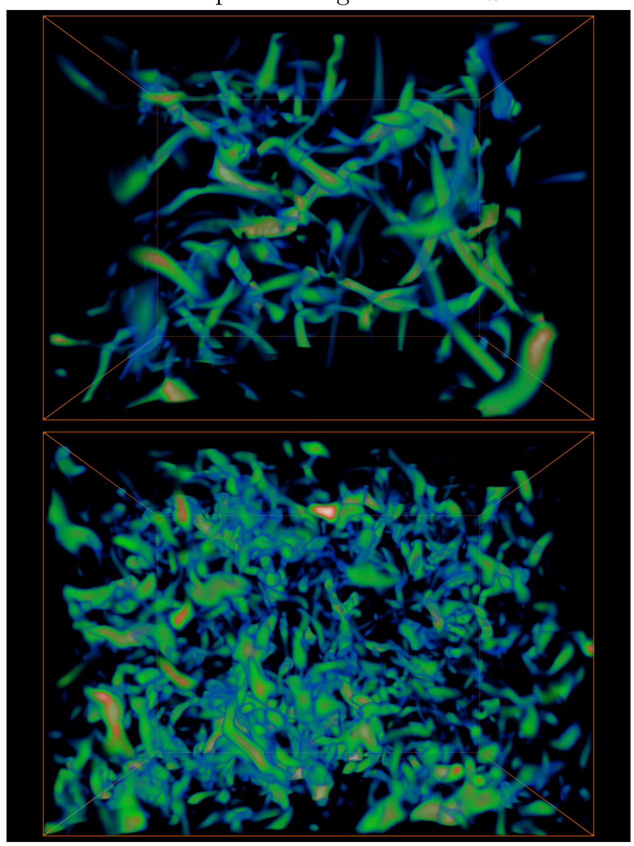

Fig. 1. Two contrasting visualizations of homogeneous, compressible turbulence as computed on a 1024^3 grid with the PPM scheme in 1993. In the upper panel, vorticity structures near the dissipation range of length scales are shown in a small region of the fully developed turbulent flow. In the lower panel, the data has been filtered before the vorticity image was rendered. These vorticity structures are in the Kolmogorov inertial range of length scales. Each region shown is the same width relative to that of the vortex tubes it contains. The two images here were rendered for direct and unbiased comparison. In each sub-volume shown, the same volume fraction is occupied by each opacity/color level. The very different appearance of these images therefore reflects real differences in their dynamics. The relatively straight vortex tubes near the dissipation range do not readily kink to form still smaller structures.

key feature of this system, aside from its very low cost (it cost us nothing), was its tremendous memory capacity, which made it the only system in the world at the time that was capable of carrying out a turbulence simulation on a 1024^3 grid. Some results of this simulation are shown in Figure 1 (see also [12-14,16, 22,23,25]). Unfortunately, the SGI personnel had to dismantle this system and distribute its components to customers before we could compute long enough to let the velocity power spectrum completely settle. It was not until 1997, using a new ASCI computer system at Los Alamos, in collaboration with Karl-Heinz Winkler and Steve Hodson, that we were at last able to calculate this flow completely. Using a new Itanium-based cluster system at NCSA in 2001 we were able to do a similar computation, this time at Mach 1, and to bring a complete, detailed set of data over the Internet to our lab in Minnesota [30,31,33]. In 2003, we were able, on a new Itanium cluster at NCSA, to simulate Mach 1 homogeneous turbulence with PPM on a grid of 2048^3 cells [34,35].

The images in Figure 1 show the difference in the structures that develop in the near dissipation range and in the Kolmogorov inertial range. Since the Fourier transform of a line vortex has a k^{-1} spectrum, it is not surprising to find spaghetti-like structures in the near dissipation range. In order to get a clear view of the structures in the inertial range, we applied a Gaussian filter to the data from this run, thus removing the spaghetti structures and letting the macaroni-like structures of the inertial range come clearly into view. Here we still see vortex tubes, but they are shorter and they appear to kink much more easily.

3. Purpose of the Simulations: Validation and Testing of Turbulence Models

The principal purpose of our turbulence simulations has been to create data sets which can be regarded in much the same way as experimental data, except that the simulations make possible the capture of data that is more complete and more detailed than is now possible from laboratory experiments. From our recent PPM simulation of Mach 1 homogeneous turbulence on a 2048^3 grid, for example, we get values of all fluid state variables sampled at 8.6 billion locations at regular time intervals (see our description of the data handling in [35]). From this data we can build grids of macrocells, each a cube of 32, 64, or even 128 grid cells on a side, in which we have computed in detail the “subgrid-scale” turbulence. From this data we can correlate the amount of subgrid turbulence and its time rate of change with the local character of the flow on larger scales and compare these results with the predictions or assumptions of turbulence closure models. In order to do this with confidence, we need to establish the range of scales on which the dissipation of the PPM gas dynamics scheme has a significant effect.

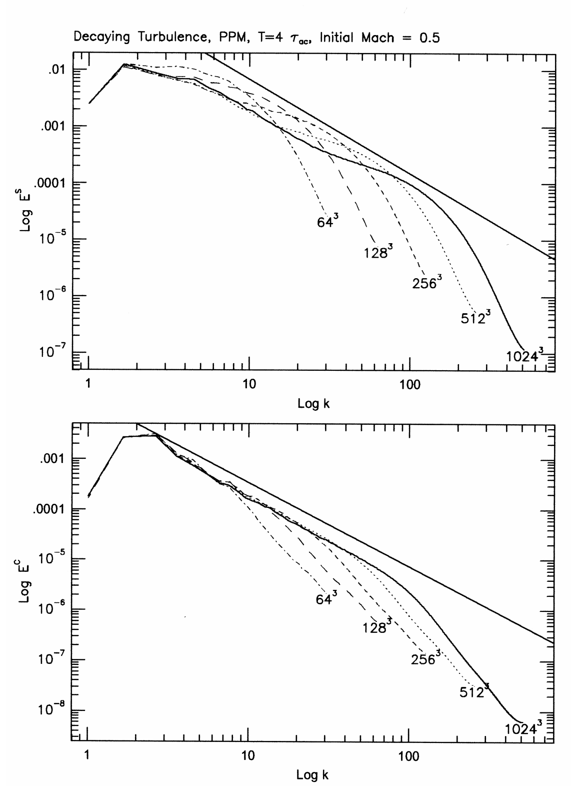

Fig. 2. Power spectra of the solenoidal (top) and compressional velocity fields in a series of PPM simulations of the same Mach ½ (rms) decaying, homogeneous, compressible turbulence problem carried out on grids of 64^3, 128^3, 256^3, 512^3, and 1024^3 cells.

If our macrocells are large enough, the effects of this dissipation on the flow on scales resolved by the macrocells should be minimal. On a fine enough grid, we will be able to have the flow on the macrogrid be essentially inviscid, while at the same time the flow we have computed inside each macrocell may still be essentially inviscid on the largest sub-macrogrid scales. A test of a turbulence model could then be constructed, in which the model is used in a large eddy simulation on the macrogrid, or perhaps on a grid finer than this by a small factor (2 or 4), and the results are compared to the macrogrid data from the 2048^3 PPM run plus the statistical properties of the sub-macrogrid-scale turbulence directly computed in that run. To be of value, such a large eddy simulation would have to come closer to the data from the 2048^3 run than a simple Euler calculation with a code like PPM using the same, coarser grid as the run with the turbulence model. Such a test remains to be performed, but now we have the data that makes such testing possible.

In order to determine the range of scales in our simulations with PPM that are essentially unaffected by the dissipation of this numerical scheme, we have performed grid resolution studies in both 2D [8] and 3D [26]. In these studies we have taken a single initial condition and computed its evolution with both the standard PPM Euler scheme described in this book and with this scheme to which the Navier-Stokes dissipation terms, for a Prandtl number of unity, have been added. For each numerical scheme, we have progressively refined the grids and computed to the same final time level. For the Navier-Stokes runs, in which there is a coefficient of viscosity to be chosen, we have used the smallest values for which a grid refinement, keeping this coefficient constant, will yield essentially the same velocity power spectrum in the computed result on the finer grid. As the grid is progressively refined, higher and higher Reynolds numbers can be reached.

It is the purpose of an Euler scheme to produce an approximation to the limit as the Reynolds number goes to infinity of well resolved Navier-Stokes simulations. On any particular grid, one may compare the closeness to this limit solution, to the extent that it can be known, of either the highest Reynolds number flow that can be correctly computed from the Navier-Stokes equations on that grid or of the Euler flow that can be computed on that grid. Our convergence studies essentially yield this comparison. If we take either the highest resolution Euler or Navier-Stokes solution as our best approximation to the desired infinite Reynolds number limit, then we need only compare Euler and Navier-Stokes runs at any of the coarser grid levels. By this measure we find that the Euler solutions are better approximations to the high Reynolds number limit on a given grid than are the Navier-Stokes solutions. This of course is no surprise, since the Euler scheme is designed to approximate this limit, while the Navier-Stokes solution is not. It is also apparent from these resolution studies that both limit sequences, that of the progressively finer Euler simulations and that of the progressively higher Reynolds number Navier-Stokes flows, approach the same limit, at least so far as the velocity power spectrum is concerned. The PPM simulation sequence approaches the limit faster, and for any given grid resolution has a larger range of scales in the velocity power spectrum that have actually converged to the limit to within a given tolerance.

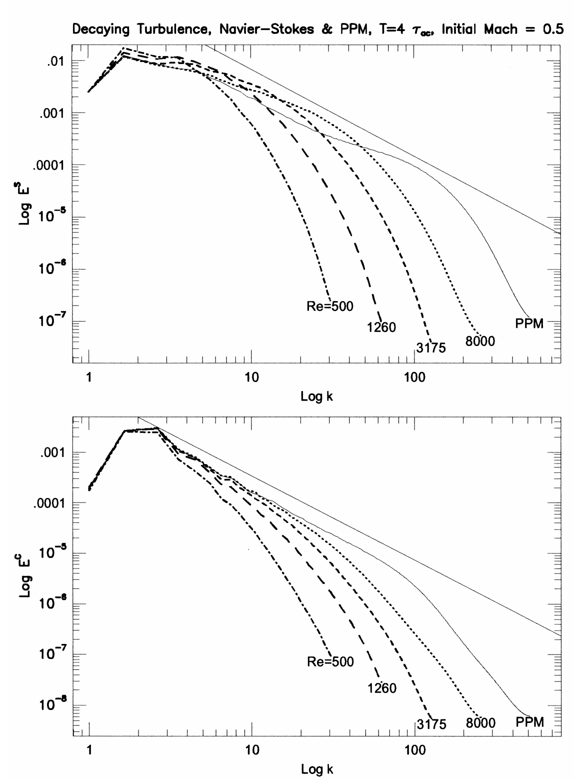

Fig. 3. Power spectra of the solenoidal (top) and compressional velocity fields in a series of PPM-Navier-Stokes simulations of the same Mach ½ (rms) decaying, homogeneous, compressible turbulence problem carried out on grids of 64^3, 128^3, 256^3, and 512^3 cells at Reynolds numbers of 500, 1260, 3175, and 8000. A PPM run with 1024^3 cells is shown for comparison.

The manner in which the velocity power spectra for the sequence of PPM runs in [26] converges is shown in Figure 2. The top panel of the figure gives the spectra for the solenoidal component of the velocity field, while the bottom panel gives spectra for the compressional component, which contains only about a tenth of the kinetic energy. The Kolmogorov trend is indicated in each panel. The flattening of the power spectrum for the solenoidal component in the near dissipation regime is clearly seen (such a flattening is not seen in our 2D resolution study [8]). As the grid is refined, this feature in the spectrum simply translates to smaller scales, while the portion of the spectrum above this feature at each grid resolution (scales larger than about 32 cell widths) is essentially converged. This same sort of behavior is seen in the compressional spectrum, except that the converged portion of the spectrum extends all the way down to a scale of about 10 to 12 cell widths. The sequence of Navier-Stokes simulations whose spectra are shown in Figure 3, also taken from [26], clearly show that a much broader portion of the spectrum on any particular grid is affected by the Navier-Stokes viscosity than is affected on that same grid by the PPM numerical viscosity. Of course, were this not so PPM would be a terrible Euler scheme, so this is no surprise. However, the Navier-Stokes spectra for the solenoidal component of the velocity field also show the flattening in the near dissipation range, so that it is clear that this feature of the turbulent velocity spectrum is physically real and not a numerical artifact. In the PPM simulations, this feature is no doubt different in detail from that of the Navier-Stokes flows; but since it is not a feature of interest for scales of reasonable size in the very high Reynolds number limit we seek to approximate, we do not regard its detailed shape as important. In fact, we can clearly see that were we to continue to refine our grid, this feature would move on down the spectrum. In this respect, it is a numerical error feature, since for the infinite Reynolds number limit it occurs at infinite, rather than any finite, wave number. Recent work of Yokokawa et al. [32] on the Earth Simulator shows this feature as well in Navier-Stokes flows that are unresolved in our sense here – that is, the coefficient of viscosity is too small for the grid resolution used – but which are computed on grids up to 4096^3.

4. Potential Role of Turbulence Models

The above results of our grid resolution studies show that motions on scales between about 12 and 32 grid cell widths are being falsified, with respect to the infinite Reynolds number limit, by the pile up of energy toward the bottom end of the turbulent cascade. The damping of motions shorter than 12 grid cell widths is a necessary feature of numerical simulation, at least for compressible

Fig. 4. Volume rendering of a thin diagonal slice through the cube of turbulence computed at NCSA in 2003 with our PPM Euler code on a grid of 2048^3 cells. The logarithm of the vorticity magnitude is shown, with the highest values of vorticity rendered as white, and with progressively smaller values rendered as yellow, red, purple, blue, and finally black. The flow is shown at 1.15 sound or flow crossing times (the initial rms velocity is Mach 1) of the energy containing scales, which are half the size of the cubical computational domain. At this stage it is clear that small-scale turbulence is developing more rapidly in some regions of this flow than in others, despite the statistical homogeneity imposed on the initial condition for the problem. Analysis of the flow on larger scales in these regions can reveal why the turbulence is developing rapidly there and not elsewhere.

flows like these that contain shocks. However, our simulations could perhaps be improved in the range of scales from 12 to 32 cell widths. If indeed the reason for the excess kinetic energy in the simulation on these scales is the difficulty of sending this energy further down the spectrum, then perhaps removing the excess on these scales via a turbulence model and placing it into a reservoir of subgrid-scale turbulence could improve the ability of the simulated flow to approximate the infinite Reynolds number limit. It is not clear that the application of a turbulence model will in fact improve the solution, since it may well matter precisely how the excess kinetic energy is removed and precisely what is done with it. For example, a simple dissipation of this excess energy directly into heat may not be helpful, since the proper flow structures on these scales of 12 to 32 cell widths are turbulent vorticity structures as shown in the lower panel of Figure 1; however, dissipation of excess kinetic energy into heat may simply leave the spaghetti-like structures of the upper panel of that figure intact, while only weakening them a bit. The convergence studies discussed above indicate that, for a given turbulent flow, if we provide enough grid cells to resolve any desired scale with 32 or more cell widths, then a PPM Euler simulation should suffice to give a good approximation to the high Reynolds number limit on those scales or larger ones. To be useful, augmentation of a scheme like PPM with a turbulence model must do better than this by giving us correct statistical flow behavior on scales smaller than 32 cell widths. That this is possible remains to be established. In short, we know that the velocity power spectrum we obtain in the near dissipation range is wrong, in the sense that the spectrum at these same wavenumbers will change upon a grid refinement, but we do not know that a turbulence model can make the description of the flow in this range right.

Not only can the data from our PPM simulations of turbulence be used to validate proposed turbulence models, the data can also point the way to formulations of such models. A key element of any such model is an equation for the rate of generation of small-scale turbulent kinetic energy in terms of the local larger-scale flow. Our turbulence simulations have such fine grids that they allow us to construct estimates of this energy transfer to small-scale motions and to visualize those estimates. Then we may seek characteristics of the regions where turbulence is growing in strength and to establish that these characteristics are indeed well correlated with growth of turbulence (i.e. they do not tend to occur elsewhere). Following this approach, we first noticed such a correlation in data from a simulation of a Richtmyer-Meshkov instability experiment [28], which we carried out as members of a large collaboration ([24,27], see also [17-21]) centered on the ASCI turbulence team at Livermore. Analyzing the 3 TB data set from this run, which was carried out on an 8 billion cell grid using our sPPM code, we noticed that the local topology of the flow was well correlated with the regions from which growing turbulent motions emerged, transported along with the local, large-scale fluid velocity [27,31,33]. These regions turned out to be those where the flow was compressing in one dimension and expanding in the other two. The time reversal of this sort of flow – compression in two dimensions and expansion in the remaining one – was correlated with decay of small-scale turbulent motions. The first sort of flow results when you clap your hands. The compression magnifies diffuse shear, and the squirting out in the other two dimensions creates shear in a thin layer even if none was originally present. The fluid instabilities that lead to turbulence are then secondary consequences of this large-scale organization of the flow. In the time-reversed case, which is a flow like the squirting of toothpaste from a tube or like the flow in a tornado, the vorticity becomes organized into tubes that tend to be aligned, so that they naturally merge into larger structures. This process leads to transport of energy up the spectrum, from small scales to larger ones. After noticing these correlations in the Richtmyer-Meshkov flow, we realized that we had been seeing them for years, without understanding their significance in this regard, in our simulations of compressible convection (see description elsewhere in this volume). In those convection flows we also saw that the intensity of turbulence was correlated with the compression of the gas in all 3 dimensions, which amplifies the vorticity and takes large-scale motions directly into smaller-scale ones by simple compression. We also saw that expansion of the convection flow in local upwellings is correlated with diminishing turbulent intensity [33].

5. Correlation of the Action of a Turbulent Cascade with the Local Flow Topology.

To see the relation between the rate of generation of subgrid-scale kinetic energy, which we write as F_{SGS} below, and the topology the larger-scale flow, we follow the classic Reynolds averaging approach. We apply a Gaussian filter with a prescribed full width at half maximum, L_f, to our simulation data to arrive at a set of filtered, or "resolved," variables and a set of "unresolved" state variables that fluctuate rapidly in space. For any particular state variable, Q, we define the filtered (or "resolved") value, $\overline{Q}$, by

$$\overline{Q}(x) \quad = \quad \int e^{-(k_f(x-x_1))^2} Q(x_1)\, d^3x \quad / \quad \int e^{-(k_f(x-x_1))^2}\; d^3x \,,$$

where the wavenumber of the filter, k_f, is related to the full width at half maximum, L_f, by $L_f = 1.6688/k_f$, and where the integral in the denominator is, of course, equal to $(2\pi)^{3/2}/(2k_f)^3$. The mass-weighted, or Favre, average of a state variable, Q, is denoted by $\tilde{Q}$. Manipulating the Euler equations using these definitions in order to arrive at the time rate of change of the kinetic energy in a frame moving with the filtered flow velocity, we get:

$$\begin{aligned} \frac{\partial k_{SGS}}{\partial t} \;+\; \partial_j(\tilde{u}_j k_{SGS}) \quad &= \quad \overline{\rho}\,\frac{D}{Dt}\left(\frac{k_{SGS}}{\overline{\rho}}\right) \quad = \\ &\left(\overline{p\,\partial_i u_i} \;-\; \overline{p}\,\partial_i \tilde{u}_i\right) \quad - \quad \tau_{ij}\,\partial_j \tilde{u}_i \\ &-\;\partial_j(\overline{u_j p} - \tilde{u}_j \overline{p} - \tilde{u}_i \tau_{ij} + \tfrac{1}{2}\overline{\rho\, u_i^2\; u_j} - \tfrac{1}{2}\overline{\rho\, u_i^2}\;\tilde{u}_j) \end{aligned}$$

Here k_{SGS} is the subgrid-scale kinetic energy, D/Dt denotes the co-moving time derivative, and τ_{ij} is the subgrid-scale stress (SGS) tensor,

$$\tau_{ij} = \overline{\rho\, u_i u_j} - \overline{\rho}\,\tilde{u}_i \tilde{u}_j$$

Using our simulation data we can establish the relative importance of the various terms grouped on the right in the above expression for the time rate of increase of subgrid-scale kinetic energy per unit mass in the co-moving frame. Preliminary analysis indicates that, statistically, the divergence terms tend to average out and that the first terms in brackets on the right, the $p\;DV$ work terms, also tend to have little effect on the average. However, the term

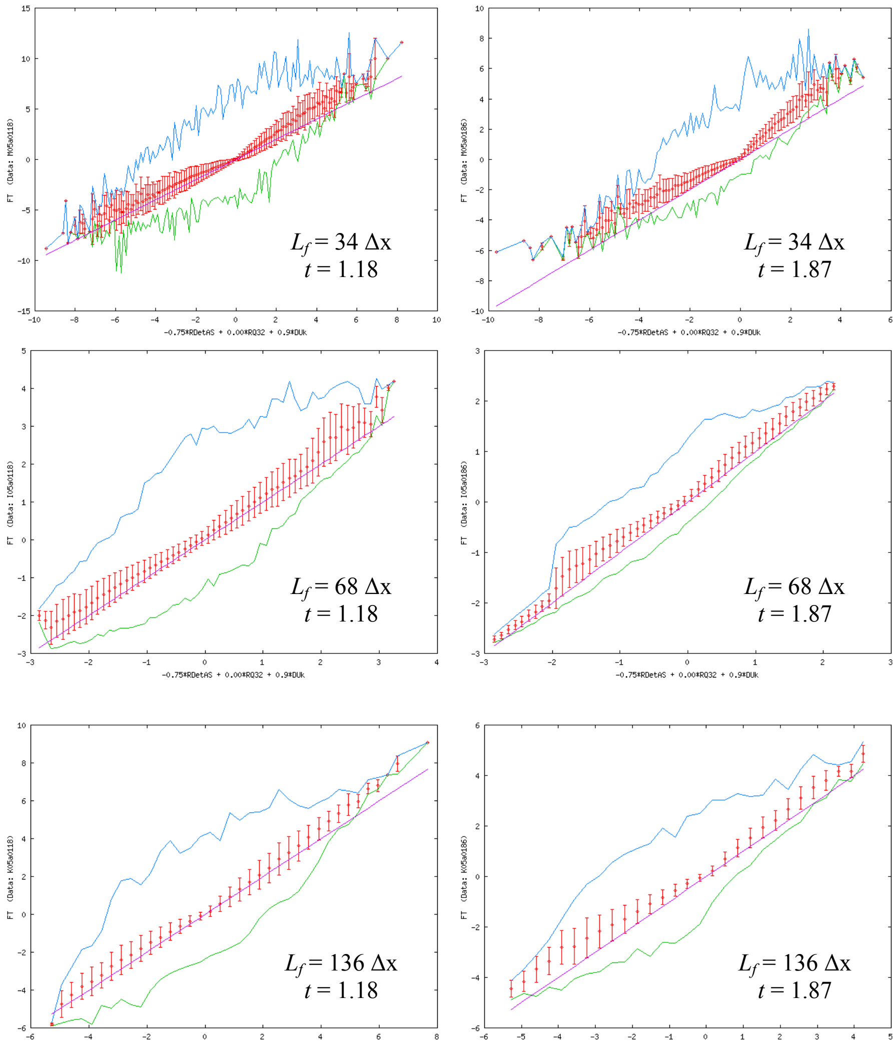

Fig. 5. Data from a PPM simulation of homogeneous, Mach 1, decaying turbulence on a grid of 2048^3 cells [34] was used to evaluate the term $F_{SGS} = -\tau_{ij}\ \partial_j \tilde{u}_i$ at 2 different times and using 3 different Gaussian filter widths. F_{SGS} is plotted above as the abcissa, and the corresponding values of the model equation discussed in the text are plotted as the ordinate. The two quantities are seen to be well correlated for this run.

$-\tau_{ij}\ \partial_j \tilde{u}_i$ has systematic behavior that tends to make it dominant over space and over time. We will refer to this term as the forward energy transfer to subgrid scales, or F_{SGS}. By analysis of several detailed data sets from PPM simulations of turbulent flows, we have correlated this F_{SGS} term to the topology of the filtered flow field, expressed in terms of the determinant of the deviatoric symmetric rate of strain tensor, given by:

$$\left(S_D\right)_{ij} \;=\; \frac{1}{2}\left(\frac{\partial \tilde{u}_i}{\partial x_j} + \frac{\partial \tilde{u}_j}{\partial x_i} \;-\; \frac{2}{3}\delta_{ij}\,\nabla\cdot\tilde{u}\right)$$

There is of course also a correlation with the divergence of this velocity field, so that a model for this forward energy transfer term results in the following form:

$$FT_{MODEL} \;=\; A\,L_f^2\,\overline{\rho}\,\det\left(S_D\right) \;+\; C\,k_{SGS}\,\nabla\cdot\tilde{u}$$

This model equation is intended for use in a large eddy simulation in which the subgrid-scale kinetic energy, k_{SGS} , is carried as an additional independent variable, so that it is available for use in the second, compressional term above. We find the best fits for the coefficients A and C in the model are:

$$A \;=\; -\,0.75\,, \qquad C \;=\; -\,0.90$$

The best fit coefficient for a term in the norm of the rate of strain tensor is zero.

The results of the above set of coefficients are shown on the previous page for data from our 2048^3 PPM simulation at 2 times during the run and for 3 choices of the filter width (the model values are along the x-axes and the actual ones along the y-axes). The fits are very good in all cases, so that we are encouraged to construct a subgrid-scale turbulence model using this model equation. Whether such a model can deliver improved simulation capabilities for our PPM code remains to be established.

6. Visual Evidence for the Correlation of F_{SGS} with $\det(S)$.

The above correlation diagrams provide quantitative confirmation of ideas that occurred to us from visual explorations of many turbulent flows. Their importance depends upon our association of the term $F_{SGS} = -\tau_{ij}\,\partial_j\tilde{u}_i$ with a useful approximation to the actual transfer of turbulent kinetic energy from the larger to the smaller scales in the flow. We therefore present below a few visual representations of fairly thin slices through a selected region of our PPM simulation of decaying Mach 1 turbulence on a 2048^3 grid. These provide qualitative, visual support for our identification of $F_{SGS} = -\tau_{ij}\,\partial_j\tilde{u}_i$ as a measure of the rate of turbulent kinetic energy transfer, and they also support the correlation of F_{SGS} with the determinant, $\det\left(\tilde{S}\right)$, of the local rate of strain tensor for the filtered velocity field. Here we do not use the deviatoric tensor, since that becomes large in shocks. In arriving at the quantitative correlations presented earlier, we sensed strong shocks in the flow and rejected results generated inside shock structures. The results presented below have been generated from data that was blended over bricks of 4^3 cells. Due to inadvertant erasure of the data from this large run by the San Diego Supercomputer Center in late 2003, a handful of such

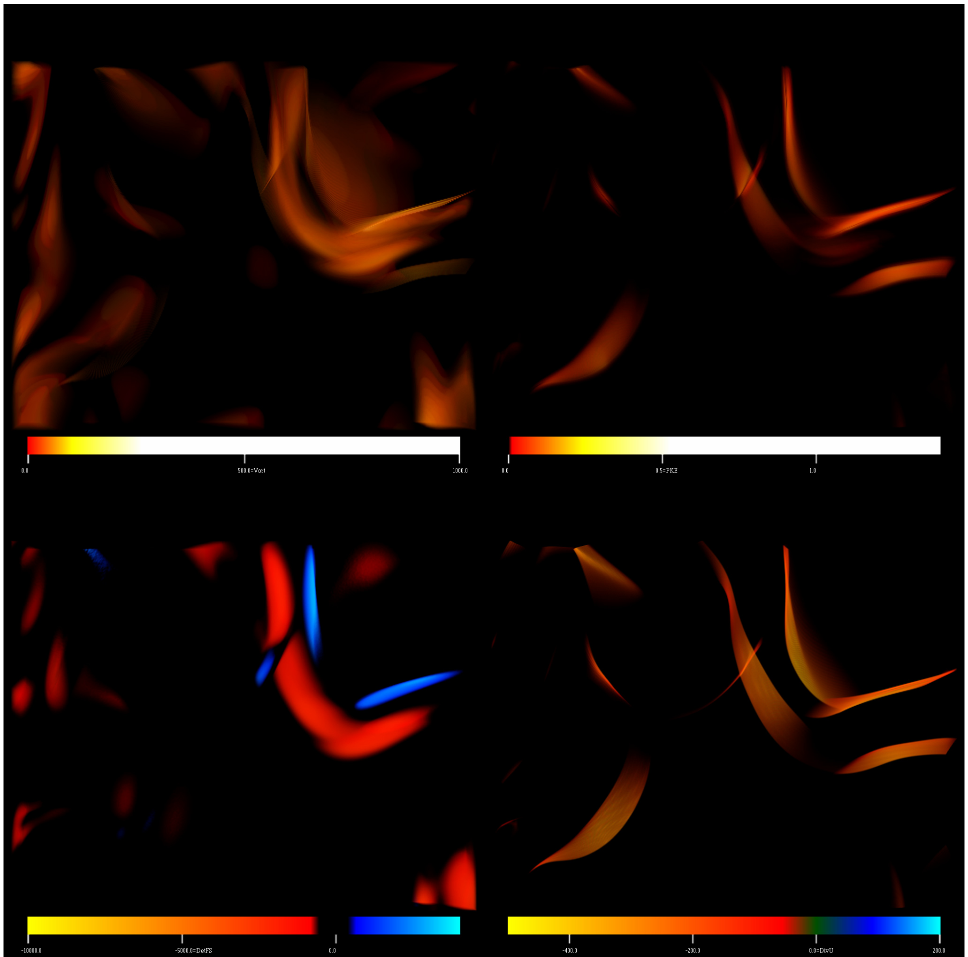

Fig. 6a. Data from a PPM simulation of homogeneous Mach 1 decaying turbulence on a grid of 2048^3 cells [34], blended over bricks of 4^3 (velocity components u_i) and 64^3 cells (velocitiy components $\tilde{u}_i$), was used to create visualizations of $|\nabla \times \vec{u}|$ (upper left), $\rho\Big((u_x - \tilde{u}_x)^2 + (u_y - \tilde{u}_y)^2 + (u_z - \tilde{u}_z)^2\Big)/2$ (upper right), $\det(\tilde{S})$ (lower left), and $\nabla \cdot \vec{u}$ (lower right) in a thin slice of the flow at time 0.30 (see text).

blended data dumps is all the quantitative data that now remains (140 detailed dumps of the vorticity distributions, sent to our lab during the run, also remain), and we are therefore forced to use this reduced resolution data here.

At each of 5 times – 0.30, 0.51, 0.71, 0.90, and 1.10 – we have plotted the magnitude of the vorticity, $|\nabla \times \vec{u}|$, generated from the averaged velocities in the bricks of 4^3 cells, in the upper left quadrant of our image panel. This quantity allows easy visual recognition of regions where small-scale turbulence is devel-

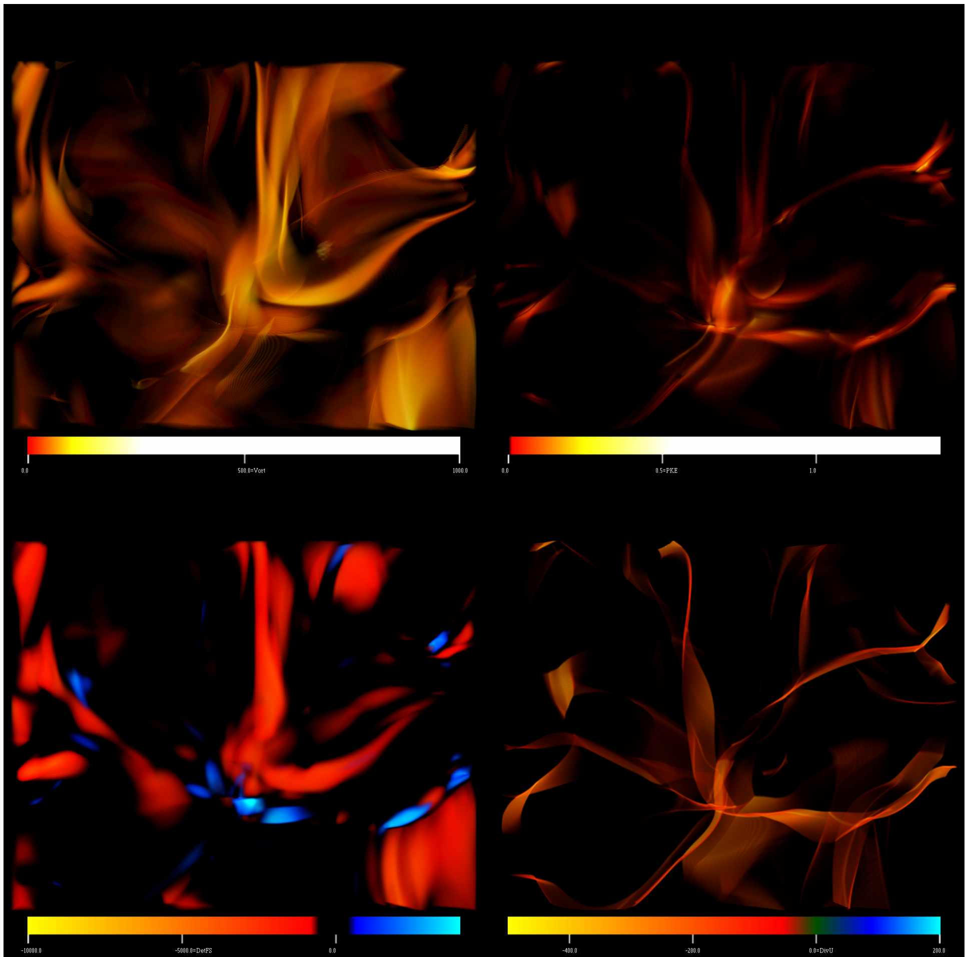

Fig. 6b. Same as Fig. 6a, but at time 0.51 (see discussion in the text).

oping. In the upper right quadrant of each image panel we show a different measure of small-scale turbulent kinetic energy, namely

$$PKE \;=\; \rho\left(u_x'^2 + u_y'^2 + u_z'^2\right)/\,2$$

where the primes denote the difference between the velocity component u_i averaged over a brick of 4^3 cells and $\tilde{u}_i$, the average of this velocity component over a brick of 64^3 cells centered on the 4^3 brick. This perturbed kinetic energy, *PKE*, is constructed so that smooth variations of $\tilde{u}_i$ do not contribute. In the lower two quadrants of each image panel, we show $\det(\tilde{S})$ at the left and $\nabla \cdot \vec{u}$ at the right. Here the divergence is constructed from the velocities, u_i, averaged over the 4^3-cell bricks, so that it gives a good representation of the shocks in this flow. The rate of strain tensor, $\tilde{S}$, defined below, is constructed

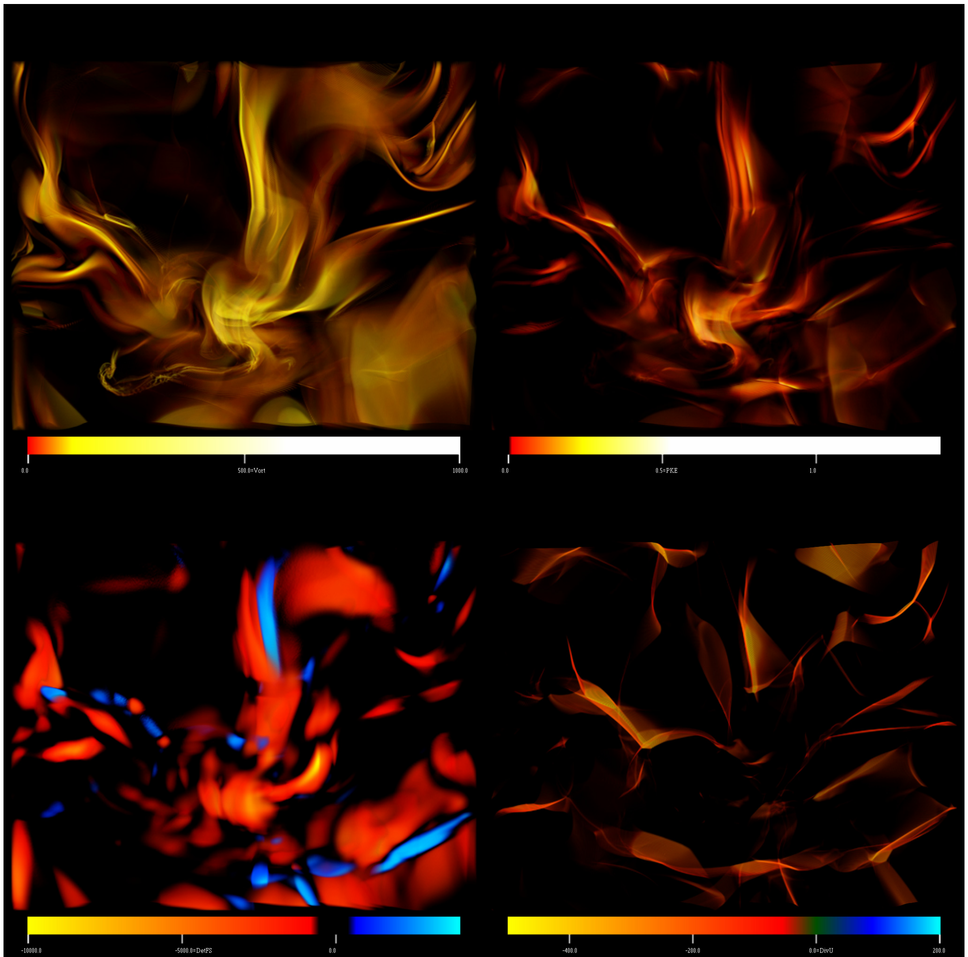

Fig. 6c. Same as Fig. 6a, but at time 0.71 (see discussion in the text).

from the velocities, $\tilde{u}_i$, averaged over 512^3 bricks of 64^3 cells each (that is, we use a moving average on 64^3 cells):

$$\tilde{S}_{ij} \;=\; \left(\partial_i \tilde{u}_j + \partial_j \tilde{u}_i\right)/2$$

This plot of $\det\left(\tilde{S}\right)$ gives us a good idea of where a turbulence model might suggest that energy is being transferred to motions on the smallest scales. If such a suggestion were to be correct, we would expect to notice this turbulent energy appearing at a later time in the plots of PKE at the upper right in each panel. We would also expect to see the tangles of small vortex tubes characteristic of fully developed turbulence appearing in the corresponding plots of the magnitude of the vorticity at the upper left.

Color versions of these figures can be found on the LCSE Web site, but even the black-and-white versions here are fairly easily interpreted, once we realize

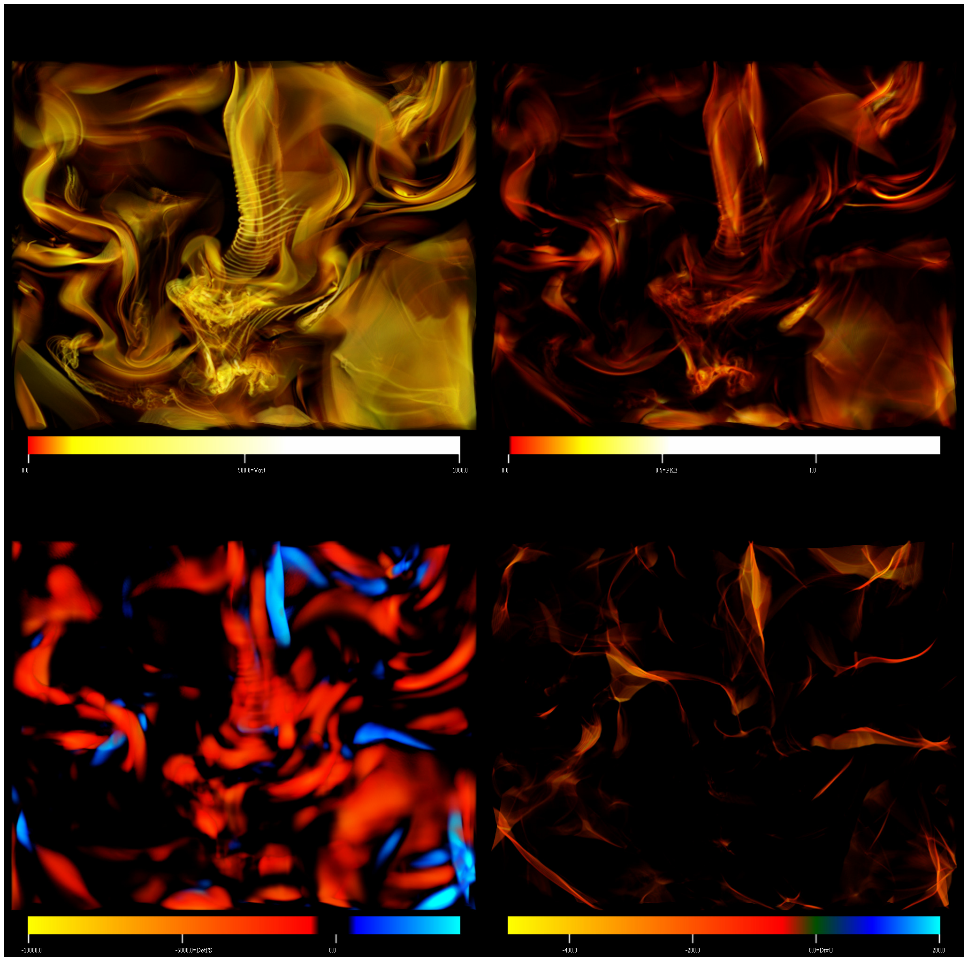

Fig. 6d. Same as Fig. 6a, but at time 0.90 (see discussion in the text).

that the positive values of the determinant $\det\left(\tilde{S}\right)$ that are rendered as blue in the color plots show up as the whitest features in black and white. Since the locations of shocks are determined during the standard PPM gas dynamics computation, it is an easy matter to set $\det\left(\tilde{S}\right)$ to zero in those locations in an implementation of a turbulence model while keeping the term in FT_{MODEL} involving the divergence of the filtered velocity active. Recognizing that, to first order, the vorticity tends to be advected with the large-scale flow, we can see from the upper-left quadrants of Figure 6 that the flow in this slice of the volume involves a stream coming from the upper right and eventually traveling through to the lower left. At time 0.30, in Fig. 6a, we see that our measure, *PKE*, of the turbulent kinetic energy is picking up false signals in strong shock fronts, which show up clearly in the plot of $\nabla \cdot \vec{u}$. At this early time, there is no small-scale

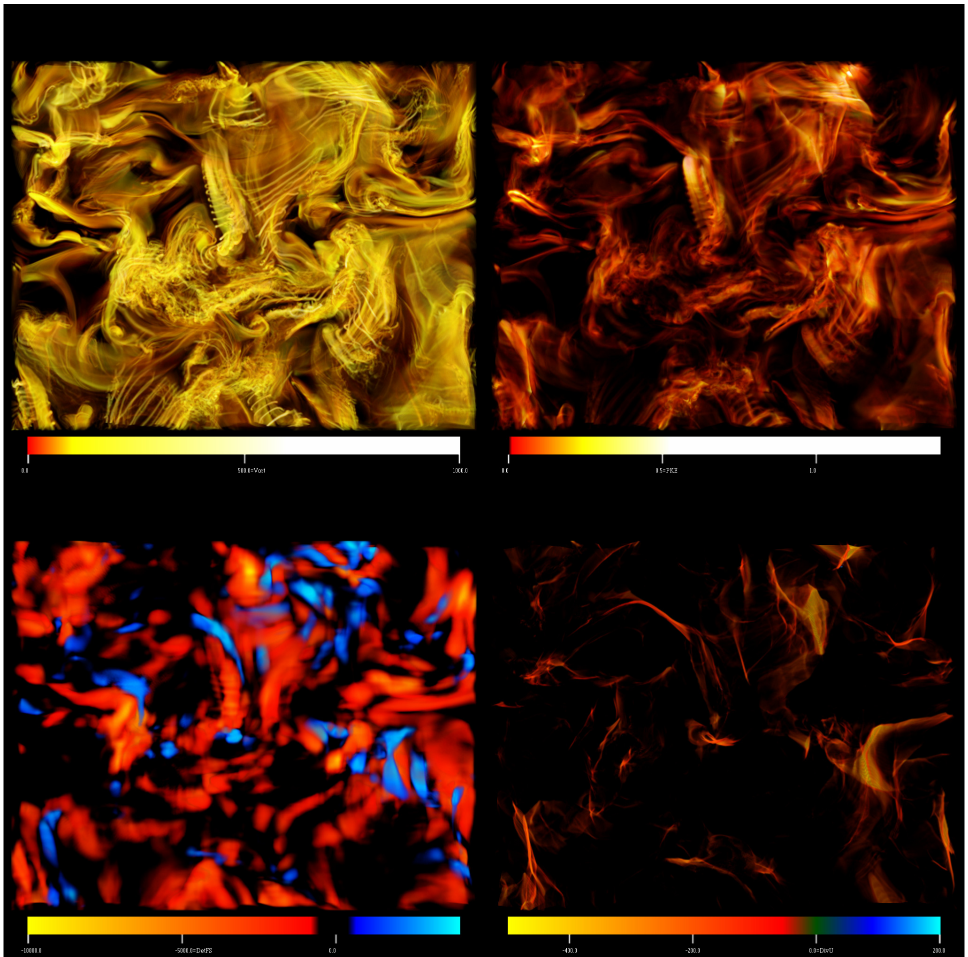

Fig. 6e. Same as Fig. 6a, but at time 1.10 (see discussion in the text).

turbulence in evidence in the vorticity plot, but we see that $\det\left(\tilde{S}\right)$ is large and negative in the region between the two roughly parallel shock fronts, where the gas is being squeezed in the direction of shock propagation but where the flow is roughly divergence free. In this same region, the shear causes a low-level, smooth feature to appear in the vorticity plot. This is not turbulence, but a precursor to turbulence that is being signaled by large negative values of $\det\left(\tilde{S}\right)$. The picture at time 0.51 is much more confused. Several strong shocks are evident. While the shearing region between the shocks at time 0.30 has now traveled into the middle of the picture, and its vorticity has intensified, there is still no small-scale turbulence. The *PKE* plot again mainly picks up false signals from the shocks, but the strong feature in $\det\left(\tilde{S}\right)$ extending from the top middle to the center of the plot and then off to the right middle is located well behind the shocks. This feature, marking gas in which conditions are ripe for the development of small-scale turbulence, is reflected in the vorticity plot, where a strong region of intensifying shear can clearly be discerned. By time 0.71 shock features no longer dominate the *PKE* plot, because small-scale turbulent features are at last beginning to emerge. The slip surface that is being driven downward and to the left by the stream of gas from the upper right is now very thin and is beginning to display a ribbed appearance from developing small-scale folds. These give rise to the strongest features in the vorticity plot, the *PKE* plot, and in the plot of $\det\left(\tilde{S}\right)$, but there are no corresponding features at all in the plot of $\nabla \cdot \vec{u}$, so we can be assured that we are not observing effects caused directly by the compressibility of the gas.

From time 0.71 onward, the large-scale flow nearly stagnates in the region of the strongest vorticity features, near the head of the stream plunging from the upper right toward the lower left. Clear evidence in the vorticity plot of small-scale turbulence is seen along the edges of this plunging flow, and corresponding features unrelated to shocks stand out in the *PKE* plots. The plots of $\det\left(\tilde{S}\right)$ indicate energy transfer to turbulence in these regions, but they also identify regions, less noticeable in the vorticity plots, where small-scale turbulence is destined later to appear. By time 1.10, several regions of positive $\det\left(\tilde{S}\right)$ have appeared. These are shown in blue in the color versions on the LCSE Web site, and they show up here as the whitest regions. Unlike the situation at earlier times, many of these regions are not correlated with shock fronts. It is natural to argue that the strength of the local shear in the filtered velocity field should be a good indicator of energy transfer to small-scale turbulence, and there is support for this view in the plots of Figure 6. However, such arguments cannot locate regions where the energy transfer runs in the opposite direction, namely from small-scale to larger-scale motions. This, we believe, is a major advantage of $\det\left(\tilde{S}\right)$ as an indicator of turbulent energy tranfer.

7. Summary.

Together with many collaborators, we have used the high resolving power and low numerical viscosity of the PPM gas dynamics scheme to simulate homogeneous, compressible, decaying turbulence in great detail. We have shown that such Euler simulations converge more rapidly to the high Reynolds number limit of viscous flows than do simulations based upon the Navier-Stokes equations. The simulations can provide high quality data for use in understanding turbulence and in guiding the development of statistical models of turbulence. In this respect, such simulations can play a role similar to experiments; but, unlike experiments, they can produce hundreds of snap shots of the flow, with all the state variables sampled at billions of locations in each one. Processing of this data is producing insights useful in the design of turbulence models.

8. References.

[1] Woodward, P. R., and P. Colella, "High-Resolution Difference Schemes for Compressible Gas Dynamics," *Lecture Notes in Phys*. **141**, 434 (1981).

[2] Woodward, P. R., and P. Colella, "The Numerical Simulation of Two-Dimensional Fluid Flow with Strong Shocks," *J. Comput. Phys*. **54**, 115-173 (1984).

[3] Colella, P., and P. R. Woodward, "The Piecewise-Parabolic Method (PPM) for Gas Dynamical Simulations," *J. Comput. Phys*. **54**, 174-201 (1984).

[4] Woodward, P. R., "Numerical Methods for Astrophysicists," in *Astrophysical Radiation Hydrodynamics*, eds. K.-H. Winkler and M. L. Norman, Reidel, 1986, pp. 245-326.

[5] Woodward, P. R., 2005. "A Complete Description of the PPM Compressible Gas Dynamics Scheme," LCSE internal report available from the main LCSE page at *www.lcse.umn.edu*.

[6] Porter, D. H., A. Pouquet, and P. R. Woodward, "Supersonic Homogeneous Turbulence," *Lecture Notes in Physics*, **392**, 105-125 (1991).

[7] Kolmogorov, A., *Dokl. Akad. Nauk SSSR,* **31**, 538 (1941).

[8] Porter, D. H., A. Pouquet, and P. R. Woodward, "A Numerical Study of Supersonic Turbulence," *Theoretical and Computational Fluid Dynamics*, **4**, 13-49 (1992).

[9] Porter, D. H., A. Pouquet, and P. R. Woodward, "Three-Dimensional Supersonic Homogeneous Turbulence: A Numerical Study," *Phys. Rev. Lett.*, **68**, 3156-3159 (1992).

[10] Porter, D. H., and P. R. Woodward, "High Resolution Simulations of Compressible Convection with the Piecewise-Parabolic Method (PPM)," *Astrophysical Journal Supplement*, **93**, 309-349 (1994).

[11] Edgar, B. K., and P. R. Woodward, "Diffraction of a Shock Wave by a Wedge: Comparison of PPM Simulations with Experiment," AIAA Paper 91-0696, and *Video Journal of Engineering Research*, **3**, 25-33 (1993).

[12] Porter, D. H., A. Pouquet, and P. R. Woodward, "Kolmogorov-Like Spectra in Decaying Three-Dimensional Supersonic Flows," *Phys. Fluids A*, **6**, 2133-2142 (1994).

[13] Woodward, P. R., "Superfine Grids for Turbulent Flows," *IEEE Computational Science & Engineering*, Vol. **1**, No. 4, pp. 4-5 (1994).

[14] Woodward, P. R., D. H. Porter, B. K. Edgar, S. E. Anderson, and G. Bassett, "Parallel Computation of Turbulent Fluid Flow," Proc. Parallel CFD '94 Conference, Kyoto, Japan, May, 1994; published in *Computing Applications Mathematics*, Vol. **14**, no. 1, pp 97-105 (1995).

[15] Silicon Graphics and the University of Minnesota, "Grand Challenge Computing, A No-Frills Technical Documentary," a video documentary produced by Silicon Graphics in October, 1993.

[16] Porter, D. H., A. Pouquet, and P. R. Woodward, "Compressible Flows and Vortex Stretching," in *Small-Scale Structures in Three-Dimensional Hydrodynamic and MHD Turbulence*, ed. A. Pouquet, M. Meniguzi, & P-L. Sulem, Springer Verlag, p. 51-58 (1995).

[17] Dannevik, W. P., A. M. Dimits, R. H. Cohen, D. Eliason, O. Schilling, D. H. Porter and P. R. Woodward, "Three-Dimensional Compressible Rayleigh-Taylor Simulation on the ASCI Blue-Pacific ID System," VHS Video (1996), LLNL Report UCRL-MI-125449.

[18] Mirin, A. A., R. H. Cohen, W. P. Dannevik, A. M. Dimits, D. E. Eliason, D. H. Porter, O. Schilling and P. R. Woodward, "Three-Dimensional Simulations of Compressible Turbulence on High-Performance Computing

Systems," Eighth SIAM Conference on Parallel Processing for Scientific Computing, Minneapolis (1997), LLNL Report UCRL-JC-125949.

[19] Schilling, O., R. H. Cohen, W. P. Dannevik, A. M. Dimits, D. E. Eliason, A. A. Mirin, D. H. Porter and P. R. Woodward, "Three-Dimensional High-Resolution Simulations of Compressible Rayleigh-Taylor Instability and Turbulent Mixing," Sixth Int'l. Workshop on the Physics of Compressible Turbulent Mixing, Marseille, France (1997), LLNL Report UCRL-JC-125308.

[20] Cohen, R. H., W. P. Dannevik, A. M. Dimits, D. E. Eliason, A. A. Mirin, D. H. Porter, O. Schilling, and P. R. Woodward, "Three-dimensional high-resolution simulations of the Richtmyer-Meshkov mixing and shock-turbulence interaction," in Proc. Of the 6th International Workshop on the Physics of Compressible Turbulent Mixing, Marseille, France, 18-21 June, 1997, pp. 128-133. LLNL Report UCRL-JC-125309.

[21] Cohen, R. H., A. M. Dimits, A. A. Mirin, W. P. Dannevik, R. G. Eastman, D. E. Eliason, O. Schilling, D. H. Porter and P. R. Woodward, "Three-Dimensional PPM Simulations of Re-shocked Richtmyer-Meshkov Instability," VHS Video (1997), LLNL Report UCRL-MI-128783.

[22] Porter, D. H., P. R. Woodward, and A. Pouquet, "Inertial Range Structures in Decaying Turbulent Flows," *Physics of Fluids* **10**, 237-245 (1998).

[23] Porter, D. H., A. Pouquet, and P. R. Woodward, "Intermittency in Compressible Flows," Proc. Seventh European Turbulence Conference, St. Jean C. F., France, July, 1998, ed. Uriel Frisch.

[24] Mirin, A. A., R. H. Cohen, B. C. Curtis, W. P. Dannevik, A. M. Dimits, M. A. Duchaineau, D. E. Eliason, D. R. Schikore, S. E. Anderson, D. H. Porter, P. R. Woodward, L. J. Shieh, and S. W. White, "Very High Resolution Simulation of Compressible Turbulence on the IBM-SP System," Lawrence Livermore National Laboratory Report UCRL-MI-134237, July, 1999.

[25] Porter, D. H., A. Pouquet, I. Sytine, and P. R. Woodward, "Turbulence in Compressible Flows," *Physica A* **263**, 263-270 (1999).

[26] Sytine, I. V., D. H. Porter, P. R. Woodward, S. W. Hodson, and K.-H. Winkler 2000, "Convergence Tests for Piecewise Parabolic Method and Navier-Stokes Solutions for Homogeneous Compressible Turbulence," *J. Comput. Phys.*, **158**, 225-238 (2000).

[27] Cohen, R. H., W. P. Dannevik, A. M. Dimits, D. E. Eliason, A. A. Mirin, Y. Zhou, D. H. Porter, and P. R. Woodward, "Three-Dimensional Simulation of a Richtmyer-Meshkov Instability with a Two-Scale Initial Perturbation," *Physics of Fluids*, **14**, 3692-3709 (2002); also available as LLNL Preprint UCRL-JC-144836 (2000).

[28] Vetter, M., and Sturtevant, B., 1995. "Experiments on the Richtmyer-Meshkov Instability of an Air/SF6 Interface," *Shock Waves*, **4**, 247-252.

[29] Porter, D. H., Pouquet, A., and Woodward, P. R., "Measures of Intermittency in Driven Supersonic Flows," *Pysical Review E* **66**, 026301 (2002).

[30] Green, K., 2001. "Going with the Flow," NCSA *Access* Magazine, Fall 2001, available at www.ncsa.uiuc.edu/News/Access/Stories/itaniumflow.

[31] Woodward, P. R., D. H. Porter, I. Sytine, S. E. Anderson, A. A. Mirin, B. C. Curtis, R. H. Cohen, W. P. Dannevik, A. M. Dimits, D. E. Eliason, K.-H. Winkler, and S. W. Hodson, "Very High Resolution Simulations of Compressible, Turbulent Flows," in *Computational Fluid Dynamics,*

Proc. of the 4th UNAM Supercomputing Conference, Mexico City, June, 2000, edited by E. Ramos, G. Cisneros, R. Fernández-Flores, A. Santillan-González, World Scientific (2001); available at *www.lcse.umn.edu/mexico*.

[32] Yokokawa, M., Itakura, K., Uno, A., Ishihara, T., and Kaneda, Y., "16.4 Tflops Direct Numerical Simulation of Turbulence by a Fourier Spectral Method on the Earth Simulator," Proc. Supercomputing 2002, Baltimore, Nov., 2002.

[33] Woodward, P. R., Porter, D. H., and Jacobs, M., "3-D Simulations of Turbulent, Compressible Stellar Convection," in *3D Stellar Evolution*, S. Turcotte, S. C. Keller, and R. M. Cavallo, eds., *ASP Conf. Series*, Vol. **293**, 45-63 (2003); available at *www.lcse.umn.edu/3Dstars*.

[34] Woodward, P. R., Anderson, S. E., Porter, D. H., and Iyer, A., "Cluster Computing in the SHMOD Framework on the NSF TeraGrid," LCSE internal report, April, 2004, available on the Web at *www.lcse.umn.edu/-turb2048*.

[35] Porter, D. H., P. R. Woodward, and A. Iyer, "Initial experiences with grid-based volume visualization of fluid flow simulations on PC clusters," accepted for publ. in Proc. Visualization and Data Analysis 2005 (VDA2005), San Jose, CA, Jan., 2005.

[36] LCSE movies from a variety of turbulent fluid flow simulations can be downloaded and/or viewed at *www.lcse.umn.edu/MOVIES*.